Asymmetric Voltage Vector-based Initial Rotor Position Detection in Four-switch Inverter Fed BLDC Motors

Xinmin Li, *Member, IEEE*, Kun Liu, Lu Zhou, Tingna Shi, *Senior Member, IEEE*, and Wei Chen, *Member, IEEE*

***Abstract*—In position-sensorless brushless direct current (DC) motors (BLDCMs) fed by a four-switch three-phase (FSTP) inverter, only two phases are fully controlled, while the remaining phase is tied to the midpoint of the split DC-link capacitors. The voltage pulses required by inductance-based initial position detection can cause unequal discharge of the series capacitors, shifting the neutral-point voltage away from half of DC-link voltage (U_{dc}/2). This neutral-point drift breaks the spatial symmetry of the inverter voltage vectors, so the 360° electrical period can no longer be evenly partitioned into six sectors during initial rotor position detection. To address this issue, this paper proposes a detection-pulse injection sequence that explicitly accounts for the asymmetric voltage vectors of the FSTP inverter. With the proposed sequence, the initial rotor position can be identified within a 30° electrical sector. The method requires no additional voltage or current sensors, and experimental results confirm its feasibility.**

***Index Terms*—Brushless direct current (DC) motor (BLDCM), Four-switch three-phase (FSTP) inverter, Asymmetric voltage vector, Initial position detection.**

I. INTRODUCTION

BRUSHLESS direct current (DC) motors (BLDCMs) feature a simple structure, high power density, and high efficiency, and are therefore widely used in servo systems and unmanned aerial vehicles [1]-[5]. Stable BLDCM operation typically relies on rotor position information provided by position sensors. However, these sensors increase system size and wiring complexity, reduce reliability, and constrain operation in harsh environments [6]-[7].

Position-sensorless control generally involves two stages: initial rotor position detection at standstill and rotor position estimation during rotation. Rotation-stage methods mainly include the back electromotive force (back-EMF) method, flux-linkage method, and inductance method [8]-[9]. Because back-EMF is negligible at standstill, it cannot provide the initial rotor position. Common standstill detection approaches include pre-positioning and inductance-based methods. The pre-positioning method applies a constant voltage vector to force the rotor to a predefined position, which inevitably causes reverse rotation. In contrast, the inductance method injects short voltage vectors into the stator windings and infers the inductance of each phase from the resulting current response, enabling initial position detection without reverse motion.

For BLDCM drives using a conventional six-switch three-phase (SSTP) inverter, several test voltage pulses are typically injected and the corresponding current amplitudes are compared, allowing the initial rotor position to be identified within a 60° electrical sector [10]. By comparing the floating-phase terminal voltage under different voltage vectors and combining this with the phase-current peak, the initial position can likewise be located within a 60° sector [11]. These methods exploit the magnetization/demagnetization effect of permanent-magnet flux on the armature flux at different rotor positions; however, their sensitivity is limited because the inductance variation with rotor angle is usually small [12]. To improve resolution, three voltage vectors can be applied sequentially while sampling the DC-link current at specific instants; together with a terminal-voltage comparison circuit, this enables initial position detection within a 30° electrical sector [13].

In practical motor drives, the switching devices of SSTP inverters are the components most susceptible to faults. A short-circuit or open-circuit fault can disable normal operation. To enhance reliability, a common fault-tolerant strategy is to reconfigure the drive into a four-switch three-phase (FSTP) topology after an SSTP fault is detected, thereby maintaining short-term operation [14]-[15]. As shown in Fig. 1, when a fault occurs in one inverter leg (e.g., phase

Manuscript received December 17, 2025; revised January 27, 2026; accepted February 25, 2026. Date of publication March 25, 2026; Date of current version March 23, 2026.

This work was supported in part by the National Natural Science Foundation of China under Grant 52477060, in part by the Tianjin Natural Science Foundation Project under Grant 24JCZDJC00250, and in part by the Zhejiang Leading Innovation and Entrepreneurship Team Project under Grant 2024R01012.

Xinmin Li, and Wei Chen are with the School of Electrical Engineering, Tiangong University, Tianjin 300387, China, and also with the Zhejiang University Advanced Electrical Equipment Innovation Center, Hangzhou 311107, China (e-mail: lixinmin@tju.edu.cn; chen_wei@tiangong.edu.cn).

Kun Liu is with the School of Electrical Engineering, Tiangong University, Tianjin 300387, China (e-mail: liukun@tiangong.edu.cn).

Lu Zhou is with the School of Electrical and Information Engineering, Tianjin University, Tianjin 300072, China (e-mail: lu_zhou@tju.edu.cn).

Tingna Shi is with the College of Electrical Engineering, Zhejiang University, Hangzhou 310027, China (e-mail: tnshi@zju.edu.cn).

(*Corresponding Author*: *Wei Chen*)

Digital Object Identifier 10.30941/CESTEMS.2026.00005

c), the corresponding motor phase can be connected to the midpoint of the split DC-link capacitors through a bidirectional thyristor (TR_c), thereby reconfiguring the drive into an FSTP inverter. This post-fault reconfiguration bypasses the faulty leg and allows the system to preserve the fundamental voltage synthesis capability and maintain (degraded) operation under power-device fault conditions. Compared with the conventional SSTP inverter, the FSTP employs only four fully controllable switches, which simplifies the inverter topology and gate-drive circuitry. However, this simplification comes at the cost of fewer available voltage vectors and an asymmetric voltage-vector distribution in the voltage plane [16]-[18].

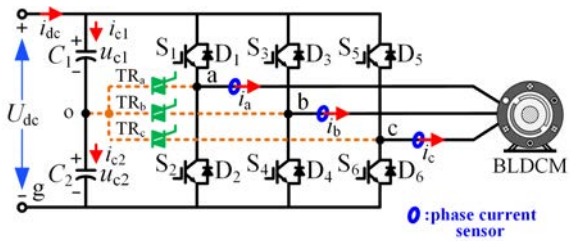

Fig. 1. BLDCM drive using a traditional SSTP inverter with fault-tolerant capability.

Although the FSTP fault-tolerant topology has been widely adopted, its asymmetric voltage vectors and the absence of natural zero vectors introduce new challenges for motor starting. Reference [19] analyzed FSTP operating modes, derived an electromagnetic-torque predictive model, and proposed a model-predictive direct-torque-control strategy to select optimal vectors for torque-ripple reduction. However, the smaller magnitude of the available vectors inherently limits the operating range. To mitigate current distortion, an improved dual-vector model-predictive control strategy was presented in [20]; visual analysis under DC-link voltage fluctuation showed reduced current distortion and improved reliability. For rotational restart under capacitor-voltage imbalance, [21] proposed dual effective-vector injection with real-time correction of vector durations, enabling accurate zero-vector synthesis and improved position-detection accuracy. Nevertheless, this method estimates rotor position from back-EMF-induced short-circuit current and thus cannot operate at low speed or standstill.

Existing standstill detection methods are largely designed for six-switch inverters with symmetrically distributed voltage vectors. They determine the initial rotor position by comparing current responses to symmetric vectors to infer relative phase inductances. In an FSTP inverter, however, the neutral-point voltage of the split DC-link capacitors is easily affected by injected vectors. Repeated injection of detection pulses can drive the neutral-point voltage away from half of DC-link voltage ($U_{dc}/2$), further disturbing the symmetry of the voltage vectors [22]-[25]. Consequently, conventional initial position detection schemes developed for SSTP inverters are generally unsuitable for BLDCMs driven by FSTP inverters.

To address this issue, this paper proposes an asymmetric-voltage-vector-based detection-pulse injection method for position-sensorless BLDCMs supplied by an FSTP inverter. The proposed approach identifies the initial rotor position within a 30° electrical sector.

II. Brushless DC Motor System Fed by a FSTP Inverter

A. Equivalent Circuit Analysis

The equivalent circuit of the BLDCM drive with an FSTP inverter is shown in Fig. 2(a). Phases a and b are healthy, whereas phase c is faulty and connected to the midpoint of the series DC-link capacitors C_1 and C_2. The DC-link voltage and current are denoted by U_{dc} and i_{dc}, respectively; u_{c1} and u_{c2} are the voltages across C_1 and C_2, respectively; and S_1-S_4 are the insulated gate bipolar transistor (IGBT) switches. The corresponding inverter output voltage vector is denoted by $\boldsymbol{V}(s_1s_2s_3s_4)$.

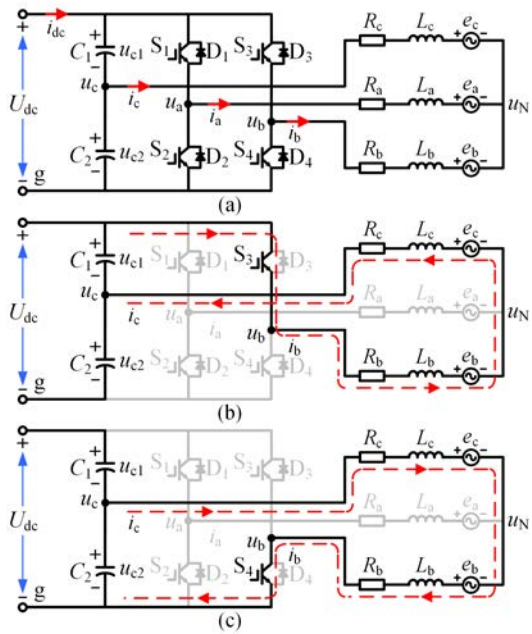

Fig. 2. Equivalent circuits of the FSTP-fed BLDCM. (a) Topology. (b) Voltage vector $\boldsymbol{V}(0010)$. (c) Voltage vector $\boldsymbol{V}(0001)$.

Taking the potential at node g as the reference (zero) level, the three-phase terminal voltages of the motor can be written as:

$$\begin{cases} u_a = R_a i_a + L_a \dfrac{di_a}{dt} + e_a + u_N \\ u_b = R_b i_b + L_b \dfrac{di_b}{dt} + e_b + u_N \\ u_c = R_c i_c + L_c \dfrac{di_c}{dt} + e_c + u_N \end{cases} \tag{1}$$

where i_k and u_k (k = a, b, c) are the motor phase current and terminal voltage, respectively; The phase resistances are $R_a = R_b = R_c = R$; L_a, L_b, and L_c are the equivalent inductance of the three-phase winding of the motor, respectively; e_a, e_b, and e_c are the three-phase back-EMF of the motor, respectively, and u_N is the neutral point voltage of the motor.

B. Output Voltage Vectors of the FSTP Inverter

Let the switching states of the four IGBTs in the FSTP

inverter be s_1, s_2, s_3, and s_4, where 1 denotes an ON state and 0 denotes an OFF state.

As shown in Fig. 3(a), the voltage vectors of a conventional SSTP inverter are symmetrically distributed, dividing one electrical cycle into six equal sectors. Here, ***V***(XXXXXX) represents the voltage vector corresponding to the switching state of the six switches in the SSTP inverter, where "1" and "0" represent the ON and OFF states of the switches, respectively. Assuming balanced DC-link capacitors (u_{c1} = u_{c2}), when only one IGBT in the two healthy phases conducts, four voltage vectors ***V***(1000), ***V***(0010), ***V***(0100), and ***V***(0001) are generated in the stationary reference frame (red arrows in Fig. 3(b)). When two IGBTs in the healthy phases conduct simultaneously, another four vectors ***V***(1001), ***V***(1010), ***V***(0110), and ***V***(0101) are produced (blue arrows in Fig. 3(b)). Under ideal balanced conditions, the six vectors ***V***(0010), ***V***(0110), ***V***(0100), ***V***(0001), ***V***(1001), and ***V***(1000) (green extensions in Fig. 3(b)) partition the electrical period into six equal sectors.

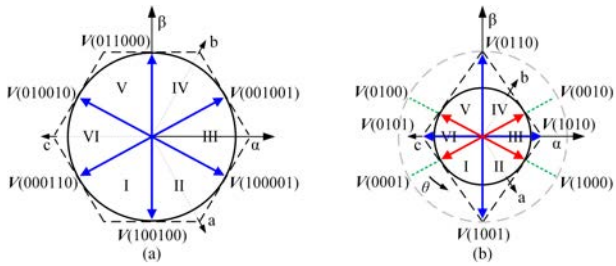

Fig. 3. Ideal voltage-vector distributions of different inverters. (a) SSTP inverter. (b) FSTP inverter.

As illustrated in Fig. 2(b), when the inverter outputs the voltage vector ***V***(0010), capacitor C_1 is discharged; similarly, Fig. 2(c) shows that C_2 is discharged when ***V***(0001) is applied. Due to practical factors such as limited DC-link capacitance, impedance mismatch, and current freewheeling, repeated application of these opposite vectors with identical pulse widths causes the split-capacitor voltages to drift from $U_{dc}/2$, i.e., $u_{c1} \neq u_{c2}$. Taking $u_{c1} > u_{c2}$ as an example, the resulting practical voltage-vector distribution is shown in Fig. 4(b).

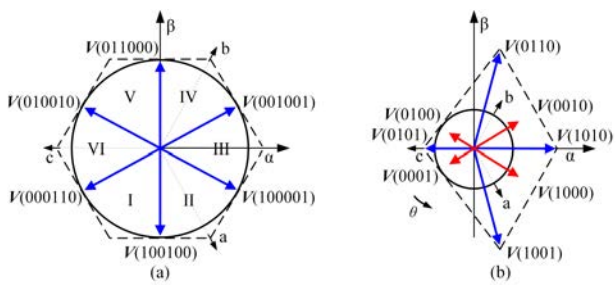

Fig. 4. Practical voltage-vector distributions of different inverters. (a) SSTP inverter. (b) FSTP inverter.

It should be clarified that the term "asymmetry" discussed in this paper encompasses two distinct aspects corresponding to the two scenarios illustrated in Figs. 3 and 4:

1) Amplitude asymmetry: As shown in Fig. 3(b), distinct from the uniform amplitude distribution of SSTP inverters, the FSTP topology itself generates voltage vectors with unequal amplitudes—specifically, the short red vectors and long blue vectors—even under capacitor voltage balance conditions.

2) Phase angle asymmetry: As illustrated in Fig. 4(b), capacitor voltage imbalance ($u_{c1} \neq u_{c2}$) induces a drift in the phase angles of the synthesized vectors, disrupting the ideal 60° spatial symmetry. The proposed detection method is specifically designed to address these asymmetries.

The proposed detection method is specifically designed to address these asymmetries.

III. New Detection-Pulse Injection Sequence

A. First Stage: Locating the Initial Rotor Position in Two 30° Electrical Ranges

Because the voltage vectors of an FSTP inverter become asymmetric under DC-link capacitor imbalance, the conventional inductance-based scheme relying on six evenly spaced vectors cannot be applied. Instead, we exploit the saliency-induced second-harmonic variation of phase inductances with rotor angle. After decoupling the three-phase inductances, the equivalent phase inductances can be written as:

$$\begin{cases} L_a = 2L_{aa0} + L_{al} + 2L_{g2}\cos(2\theta) \\ L_b = 2L_{aa0} + L_{al} + 2L_{g2}\cos\left(2\theta + \dfrac{2\pi}{3}\right) \\ L_c = 2L_{aa0} + L_{al} + 2L_{g2}\cos\left(2\theta - \dfrac{2\pi}{3}\right) \end{cases} \tag{2}$$

where θ is the included angle between rotor q axis and phase a winding axis; L_{aa0} is the constant component of the motor winding self-inductance; L_{al} is the inductance component caused by leakage flux, and L_{g2} is the second harmonic amplitude of winding self-inductance. As shown in Fig. 5, the intersections of L_a, L_b, and L_c divide one electrical period into twelve 30° sectors; therefore, the initial position can be narrowed to two candidate 30° ranges separated by 180° by comparing the relative magnitudes of L_a, L_b, and L_c.

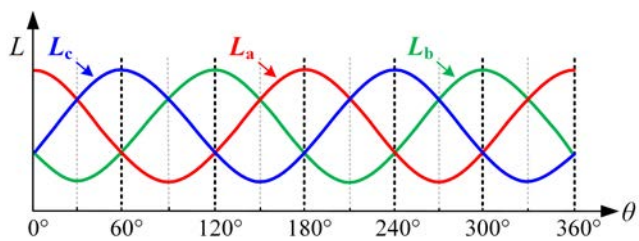

Fig. 5. Equivalent inductances of the three-phase windings versus rotor electrical angle.

1) Comparison between L_a and L_c using V(0100)

To implement the magnitude comparison of L_a and L_c, it is necessary to select voltage vectors that enable conduction solely in phases a and c. In the FSTP topology, voltage vectors ***V***(0100) and ***V***(1000) both satisfy this conduction condition. The distinction between them lies merely in the opposite direction of current flow, rendering them fully equivalent in terms of the inductance comparison principle. Without loss of generality, this paper takes ***V***(0100) as an

example for detailed analysis, as illustrated in Fig. 6(a). With $u_c = u_{c2}$, $u_a = 0$, $i_c = -i_a$, $i_b = 0$, and $e_a = e_b = e_c = 0$ at standstill, the motor neutral-point voltage is obtained from equations of phases a and c as:

$$u_N = \frac{u_{c2}}{2} + \frac{1}{2}\left(L_a - L_c\right)\frac{di_a}{dt} \tag{3}$$

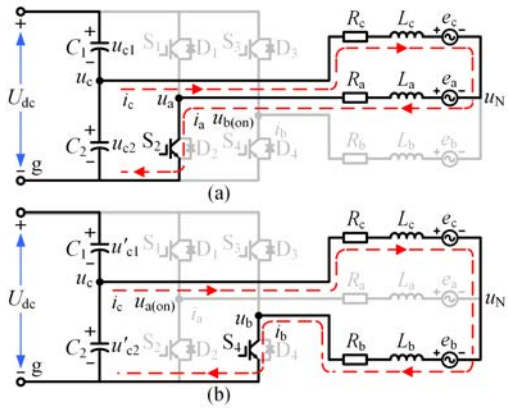

Fig. 6. Equivalent circuits under different injected voltage vectors. (a) ***V***(0100). (b) ***V***(0001).

Since phase b is floating, its terminal voltage equals the neutral-point voltage during the pulse:

$$u_{b(on)} = u_N \tag{4}$$

Combining (3) and (4) yields a direct inductance judgement rule:

$$\begin{cases} u_{b(on)} \geq \dfrac{u_{c2}}{2} \Rightarrow L_c \leq L_a \\ u_{b(on)} < \dfrac{u_{c2}}{2} \Rightarrow L_c > L_a \end{cases} \tag{5}$$

To suppress non-ideal disturbances, the comparison between $u_{b(on)}$ and $u_{c2}/2$ is sampled at the mid-pulse instant $T_s/2$, where T_s denotes the injection period. The result is recorded as the digital flag C_{Aout}, where C_{Aout} = H when $u_{b(on)} > u_{c2}/2$, and C_{Aout} = L when $u_{b(on)} < u_{c2}/2$.

2) Comparison between L_b and L_c using V(0001)

Similarly, when comparing L_b and L_c, based on the same selection principle mentioned above, both vectors ***V***(0001) and ***V***(0010) can enable conduction in phases b and c and are functionally equivalent, differing only in the direction of current flow. This paper takes ***V***(0001) as an example for detailed analysis, as shown in Fig. 6(b). Let the instantaneous lower-capacitor voltage be u'_{c2}. With $u_c = u'_{c2}$, $u_b = 0$, $i_c = -i_b$, and $i_a = 0$, the corresponding neutral-point voltage becomes:

$$u_N = \frac{u'_{c2}}{2} + \frac{1}{2}\left(L_b - L_c\right)\frac{di_b}{dt} \tag{6}$$

and the floating phase voltage satisfies:

$$u_{a(on)} = u_N \tag{7}$$

Therefore, the comparison between $u_{a(on)}$ and $u'_{c2}/2$, sampled at $T_s/2$, gives the inductance relation L_c versus L_b. The result is stored as C_{Bout}, where C_{Bout} = H when $u_{a(on)} > u'_{c2}/2$, and C_{Bout} = L when $u_{a(on)} < u'_{c2}/2$.

Note that C_2 discharges during both injections, so $u'_{c2} \neq u_{c2}$. This is exactly why vectors whose phase angles drift under capacitor imbalance (e.g., ***V***(1001) and ***V***(0110)) are avoided in the first stage.

3) Comparison between L_a and L_b using three-phase conduction

Finally, when comparing L_a and L_b, a three-phase conduction circuit needs to be constructed. Theoretically, ***V***(1001), ***V***(0110), ***V***(0101), and ***V***(1010) all satisfy the conduction condition. However, the former two connect phases a and b to the positive and negative terminals of the DC link, respectively. Under capacitor voltage imbalance, this results in $u_a \neq u_b$, making inductance comparison impossible. To eliminate the interference caused by imbalance, it is necessary to select vectors that connect phases a and b to the same DC-link potential. Both ***V***(0101) and ***V***(1010) satisfy the condition $u_a = u_b$ and are functionally equivalent. This paper takes ***V***(0101) as an example for detailed analysis, as illustrated in Fig. 7. With $u_c = u''_{c2}$, $u_a = u_b = 0$, and $i_a + i_b = -i_c$, summing the three phase equations yields:

$$u_N = \frac{1}{3}\left[u''_{c2} + \left(L_c - L_a\right)\frac{di_a}{dt} + \left(L_c - L_b\right)\frac{di_b}{dt}\right] \tag{8}$$

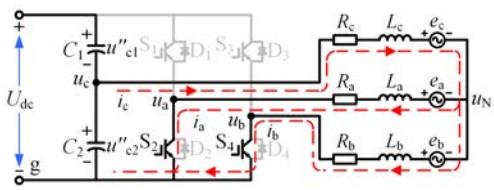

Fig. 7. Equivalent circuit of the system under the injected voltage vector ***V***(0101) (three-phase conduction state).

During the pulse, both phases a and b windings are driven by u_N. In the linear magnetic region, the equivalent inductance can be approximated by:

$$L = \frac{u}{di/dt} \approx \frac{u\Delta t}{\Delta i} \tag{9}$$

so the inductance is inversely proportional to the current slope. Let I_a and I_b be the absolute values of phase currents measured at the end of the pulse. If $I_a > I_b$, then $L_a < L_b$; otherwise $L_a \geq L_b$.

The voltage comparisons in stages I and II are implemented by the terminal-voltage comparison circuit shown in Fig. 8 (resistor divider and LM393 comparator), which generates the digital flags C_{Aout} and C_{Bout}.

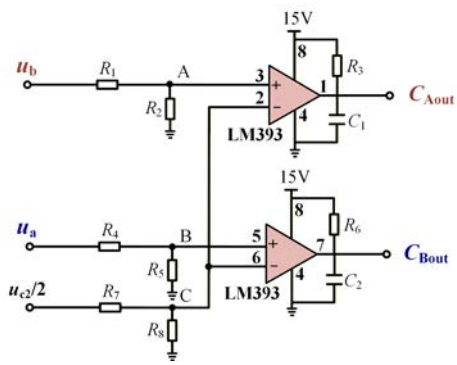

Fig. 8. Terminal-voltage comparison circuit used to generate C_{Aout} and C_{Bout}.

By sequentially applying ***V***(0100), ***V***(0001), and ***V***(0101) and evaluating (C_{Aout}, C_{Bout}, I_a, I_b), the relative order of L_a, L_b,

and L_c is obtained without being affected by capacitor-voltage imbalance. The initial rotor position is thus narrowed to two candidate 30° electrical sectors separated by 180°, which will be disambiguated in stage II.

B. Second Stage: Determining the Final 30° Sector by Polarity Identification

Stage I yields two candidate 30° sectors that are 180° apart. To resolve this ambiguity, and stage II identifies the polarity of the permanent-magnet rotor by exploiting magnetic saturation, which makes the phase inductance depend on current direction and magnitude.

When the rotor is fixed, the winding inductance can be regarded as a function of the injected current. If the current amplitude is below the saturation threshold i_{th}, the magnetic circuit is approximately linear and the equivalent inductance is L_0. Once $|i| > i_{th}$, saturation occurs and the inductance varies nonlinearly with current, which can be summarized as:

$$L(i)=\begin{cases} L_0, & |i| \le i_{th} \\ f(i,\zeta), & |i| > i_{th} \end{cases} \tag{10}$$

where ζ is a shape coefficient describing the saturation-induced inductance change.

Assuming that the total phase flux linkage is λ_{phase}, the permanent magnet (PM) flux linkage is λ_{PM}, and the current-produced flux linkage is $L(i)i$, their relationship is:

$$\lambda_{phase} = \lambda_{PM} + L(i)i \tag{11}$$

Thus, injecting a current i^+ along the PM flux produces a magnetizing effect, increasing saturation and reducing inductance to L^+; injecting i^- against the PM flux produces a demagnetizing effect, decreasing saturation and increasing inductance to L^-. Consequently,

$$L^+ < L_0 < L^- \tag{12}$$

which is consistent with the nonlinear λ-i characteristic in Fig. 9.

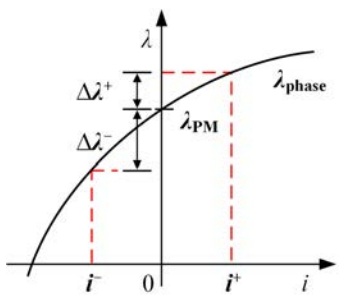

Fig. 9. Relationship between motor current and flux linkage.

Because the two candidate sectors from stage I differ by 180° (e.g., $0° < \theta < 30°$ or $180° < \theta < 210°$ when $L_a > L_c > L_b$), the polarity must be identified before selecting the final sector.

In conventional SSTP drives with a single DC-link capacitor, polarity is typically determined by applying two opposite voltage vectors with equal amplitude and comparing the end-of-pulse current according to (11). This approach implicitly relies on two properties:

1) All six active vectors are symmetrically distributed and unaffected by DC-link conditions.

2) The two opposite vectors are exactly 180° apart with identical magnitude, so any difference in current response can be ascribed solely to the magnetizing or demagnetizing action of the PM flux.

In an FSTP inverter with split DC-link capacitors, however, the capacitor-voltage imbalance ($u_{c1} \neq u_{c2}$) causes some three-phase conduction vectors (such as $\boldsymbol{V}(1001)$ and $\boldsymbol{V}(0110)$) to deviate from their nominal phase positions in the α-β plane (Fig. 4(b)). As a result, these vectors no longer form strictly opposite pairs, and the current response under two opposite vectors is influenced not only by rotor polarity but also by the instantaneous capacitor voltages.

To avoid this ambiguity, the proposed method explicitly removes all vectors, whose phase is sensitive to capacitor-voltage imbalance and restricts polarity detection to the four two-phase conduction vectors $\boldsymbol{V}(0001)$, $\boldsymbol{V}(0010)$, $\boldsymbol{V}(0100)$, and $\boldsymbol{V}(1000)$. Moreover, instead of comparing the currents obtained at the end of two different opposite vectors as in the SSTP case, the proposed scheme evaluates the current slopes at different instants within the action of a single vector. By observing how the slope evolves within one pulse (and repeating the same procedure for its counterpart vector), the method distinguishes magnetizing and demagnetizing effects without relying on perfectly opposite vector pairs.

In this way, the polarity decision is based on intra-vector slope variation under a selected subset of four usable vectors, rather than on end-of-pulse current differences between ideal opposite vectors, which are no longer guaranteed in the FSTP topology.

Specifically, after stage I, a fourth vector is applied for $2T_s$ to drive the magnetic circuit into saturation. The average current change rates at $t_1 = T_s$ and $t_2 = 2T_s$, where t_1 and t_2 denote the midpoint and the end instant of the fourth vector injection, respectively, are denoted by k_1 and k_2, respectively (Fig. 10). In practical applications, to avoid division operations, the comparison between k_1 and k_2 is equivalent to directly comparing $2i_c(t_1)$ and $i_c(t_2)$. This comparison method requires only two current sampling points per voltage vector injection, namely $i_c(t_1)$ and $i_c(t_2)$. According to (9) and (12), if the fourth vector produces a magnetizing current, the inductance decreases during saturation and the current ramps faster, giving

$$k_1 < k_2 \tag{13}$$

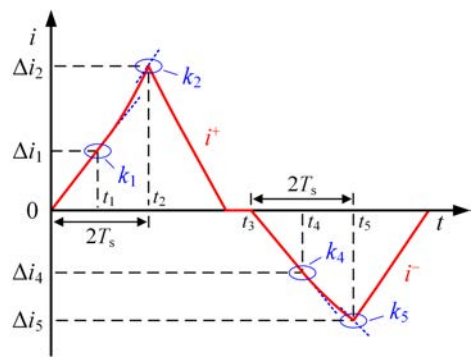

Fig. 10. Current responses under two opposite voltage vectors with different amplitudes for rotor polarity identification.

Then, a fifth vector of opposite direction and the same duration is applied, and the corresponding slopes k_4 (at $t_4 = T_s$) and k_5 (at $t_5 = 2T_s$) are obtained. If the fifth vector is demagnetizing, saturation weakens and the current ramp slows, yielding:

$$k_4 < k_5 \tag{14}$$

For example, when the rotor lies in $0° < \theta < 30°$, the optimized opposite pair is $\boldsymbol{V}(0001)$ followed by $\boldsymbol{V}(0010)$, which maximizes the saturation asymmetry; thus $k_1 < k_2$ and $k_4 < k_5$. Conversely, if the rotor lies in the opposite candidate sector $180° < \theta < 210°$, both inequalities reverse, i.e., $k_1 > k_2$ and $k_4 > k_5$.

Regarding the selection of specific voltage vectors, we adhere to the principle of maximizing the magnetic saturation effect. When the angular deviation between the direction of the injected voltage vector and the rotor flux linkage is minimized, a higher degree of magnetic saturation can be induced. This yields the most significant difference in current slopes, thereby enhancing detection sensitivity. Based on this principle, the selection of voltage vectors is illustrated in Fig. 11:

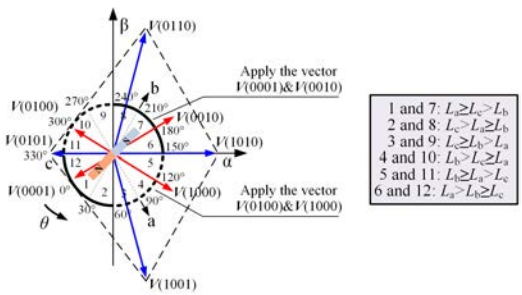

Fig. 11. Voltage vectors selected for permanent-magnet rotor polarity determination in the FSTP inverter.

If the rotor is in sector 1, 2, 6, 7, 8, 12, apply $\boldsymbol{V}(0001)$ then $\boldsymbol{V}(0010)$;

if the rotor is in sector 3, 4, 5, 9, 10, 11, apply $\boldsymbol{V}(0100)$ then $\boldsymbol{V}(1000)$.

C. Parameter Design of Pulse Injection

The voltage-vector injection timing is designed by balancing detection sensitivity and robustness. In general, a longer pulse produces a larger current response and improves sensitivity, but it also increases the likelihood of magnetic saturation, unwanted torque disturbance, and overcurrent. Therefore, the pulse duration is selected with reference to a critical saturation time threshold t_{sat}, which indicates when the magnetic circuit begins to enter saturation under the injected voltage.

For the sector-identification stage, a relatively short pulse is applied so that the current remains in the quasi-linear region ($t < t_{sat}$). This preserves the validity of the inductance-related response used for sector judgment while maintaining adequate signal-to-noise ratio for reliable detection.

For the polarity-identification stage, a longer pulse is intentionally used to drive the magnetic circuit into saturation ($t > t_{sat}$), so that saturation-induced differences in the current slope can be exploited for polarity discrimination. Meanwhile, the pulse width is constrained by a safety upper bound to prevent triggering overcurrent protection and to reduce the risk of undesired rotor motion.

The pulse interval is chosen to be comparable to the pulse duration, allowing the phase current to decay sufficiently between injections. This minimizes residual-current carryover and prevents bias in subsequent measurements, thereby improving robustness and repeatability of the overall detection process.

D. Robustness of the Proposed Method

The proposed initial position detection method exhibits robustness for practical applications, primarily because the pulse-injection timing parameters are designed according to constraints with sufficient margins. Specifically, the pulse duration is confined within an effective window. In the sector identification stage, a relatively short pulse is applied to keep the magnetic circuit in the quasi-linear region, ensuring that the inductance-related response remains reliable and preventing saturation-induced nonlinearity from corrupting the decision logic. In the polarity identification stage, a longer pulse is intentionally used to activate saturation-dependent features, while an upper safety bound is imposed to avoid overcurrent risk and excessive instantaneous torque disturbance. Since the selected pulse widths are placed away from the constraint boundaries, the injected responses remain within the discriminative region even under non-ideal conditions such as inductance dispersion and DC-link voltage fluctuations, thereby maintaining stable detection performance.

Robustness is further enhanced by a proper pulse-interval design. As the stator winding behaves as a resistance–inductance (R-L) load, the current decays through the freewheeling path after each injection. If the interval is too short, residual current will carry over into the next injection as a non-zero initial condition, leading to biased responses and systematic errors. Therefore, the interval is set sufficiently long to allow the phase current to decay adequately, suppressing residual-current accumulation and improving the consistency and repeatability of successive injections.

IV. Experimental Results and Analysis

A. Experimental Setup

The proposed initial rotor position detection method was experimentally validated on an FSTP-fed BLDCM drive prototype. A three-phase BLDCM is supplied by a four-switch inverter, in which one phase leg of the original SSTP inverter is bypassed and reconfigured to the midpoint of the split DC-link capacitors. A digital signal processor is used to implement the proposed algorithm, including the detection-pulse injection sequence and the polarity identification procedure.

Phase currents are measured by current sensors, while the terminal-voltage comparison circuit in Fig. 8 is employed to generate the digital outputs C_{Aout} and C_{Bout} for inductance comparison. For verification purposes only, a position sensor

(encoder) is mounted on the motor shaft to provide the reference rotor position; this signal is not used by the proposed algorithm. Table I lists the parameters of BLDCM and FSTP inverter.

TABLE I
THE PARAMETERS OF BLDCM AND FSTP INVERTER

Parameter	Value
Rated voltage, U_N/V	320
Rated current, I_N/A	120
Rated speed, n_N/(r/min)	3000
Rated torque, T_N/(N·m)	64
Pole pairs, p	4
Flux linkage, λ_{PM}/Wb	0.067
Stator resistance, R/mΩ	7.34
d-axis inductance, L_d/mH	0.158
q-axis inductance, L_q/mH	0.292
Capacitance, $C_1 = C_2$/μF	737

B. Behavior of DC-link Capacitor Voltages During Detection

A key motivation for developing a dedicated detection method for FSTP inverters is the DC-link capacitor voltage imbalance generated by the detection pulses themselves. To experimentally verify this effect, a given rotor position is fixed, and the five short detection vectors of the proposed algorithm are applied.

Fig. 12 shows the gate signals of the four switches and the corresponding capacitor voltages u_{c1} and u_{c2} during this sequence. The DC-link voltage is U_{dc} = 320 V. Before detection, the split DC-link is balanced, i.e., $u_{c1} = u_{c2} = U_{dc}/2$. In stage I, the three vectors $\boldsymbol{V}(0100)$, $\boldsymbol{V}(0001)$, and $\boldsymbol{V}(0101)$ are applied. Since capacitor C_2 is repeatedly discharged during these injections, u_{c2} gradually decreases while u_{c1} remains close to its initial value, leading to a clear imbalance with $u_{c1} > u_{c2}$ at the end of stage I.

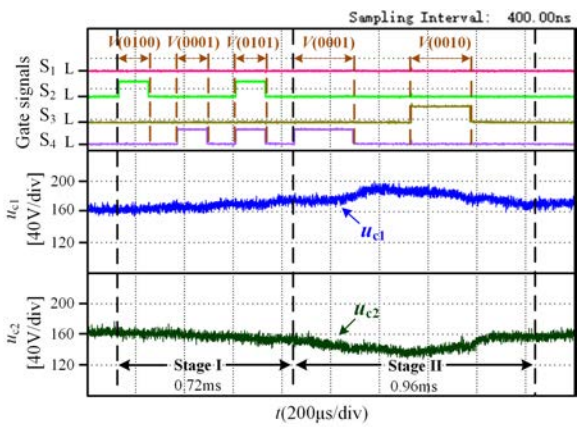

Fig. 12. Experimental waveforms of applying voltage vectors and capacitors C_1 and C_2 voltages of the proposed method.

In stage II, a pair of opposite vectors (here $\boldsymbol{V}(0001)$ and $\boldsymbol{V}(0010)$) is applied to perform polarity identification. The first vector continues to discharge C_2, further reducing u_{c2}; the second vector mainly discharges C_1, causing u_{c1} to drop and u_{c2} to recover partially. Although the imbalance is mitigated to some extent, Fig. 12 shows that u_{c1} and u_{c2} remain unequal after the full detection sequence.

These results confirm that, in the FSTP topology, the split DC-link voltages inevitably deviate from $U_{dc}/2$ during initial position detection. As a consequence, the space vectors associated with certain three-phase conduction states no longer maintain their ideal, symmetric distribution. This experimental evidence justifies the design choices in Sections II and III, namely: using only those voltage vectors that are less sensitive to capacitor-voltage imbalance and relying on terminal-voltage comparisons and intra-pulse current-slope information, rather than on symmetric-vector assumptions inherited from SSTP inverters.

C. Detection Performance at Different Initial Rotor Positions

This subsection evaluates the effectiveness of the proposed method over a wide range of initial rotor positions. All detection experiments are conducted with the motor at standstill.

Fig. 13 shows typical waveforms of the proposed method when the initial rotor position is 2° (0.03 rad). The first three vectors $\boldsymbol{V}(0100)$, $\boldsymbol{V}(0001)$, and $\boldsymbol{V}(0101)$ are applied with a duration T_s = 120 μs and an interval of 120 μs. At the mid-pulse instant t_1 of the first vector, the comparison between u_b and $u_{c2}/2$ gives C_{Aout} = H; at the mid-pulse instant t_2 of the second vector, the comparison between u_a and $u_{c2}/2$ yields C_{Bout} = L. At the end instant t_3 of the third vector, the measured current magnitudes are $|i_a|$ = 19.1 A and $|i_b|$ = 54.1 A. Based on the inductance-angle characteristics in Fig. 5, these results correspond to the ordering $L_a > L_c > L_b$, which localizes the rotor to either sector $0° < \theta < 30°$ or sector $180° < \theta < 210°$.

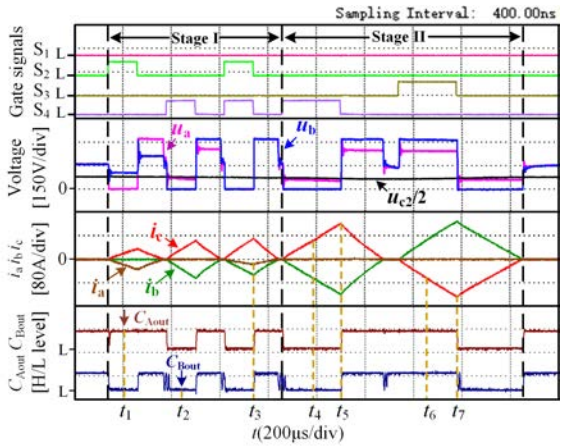

Fig. 13. Experimental waveforms with the initial rotor position locates in 2° (0.03 rad).

To determine the rotor polarity and select the correct sector, two opposite vectors $\boldsymbol{V}(0001)$ and $\boldsymbol{V}(0010)$ are then applied with a duration and interval of 240 μs. The currents of phase c at the mid and end instants of the two pulses are used to compute the average current slopes k_1, k_2, k_4, and k_5 (corresponding to t_4, t_5, t_6, and t_7, respectively) as defined in Section III-B. In this test, $k_1 < k_2$ and $k_4 < k_5$ are obtained, which indicates a specific rotor polarity. According to the decision rule, the rotor is finally identified as lying in sector 1, i.e., $0° < \theta < 30°$. During the entire detection process, the motor remains at standstill, and no reverse motion is

observed. The detailed process for detecting the initial position is summarized in Table II.

TABLE II
THE INITIAL POSITION DETECTION PROCESS IN FIG. 13

Initial position	2° (0.03 rad)				
Detection process	Stage I	$\boldsymbol{V}(0100)$	t_1	$u_b > u_{c2}/2$	C_{Aout} = H
		$\boldsymbol{V}(0001)$	t_2	$u_a < u_{c2}/2$	C_{Bout} = L
		$\boldsymbol{V}(0101)$	t_3	$\lvert i_a\rvert$ =19.1 A $\lvert i_b\rvert$ = 54.1 A	$L_a > L_b$
	Stage II	$\boldsymbol{V}(0001)$	t_4	i_c = 59.8 A	$k_1 < k_2$
			t_5	i_c = 123.9 A	
		$\boldsymbol{V}(0010)$	t_6	i_c = −69.5 A	$k_4 < k_5$
			t_7	i_c = −131.1 A	
Result	Sector 1 ($0° < \theta < 30°$)				

Fig. 14 shows the experimental waveforms at initial rotor positions of 115° (2.01 rad) and 295° (5.15 rad). As shown in Fig. 14(a), at the initial position of 115° (2.01 rad), the first three voltage vectors $\boldsymbol{V}(0100)$, $\boldsymbol{V}(0001)$, and $\boldsymbol{V}(0101)$ are applied with a duration and interval of 120 μs. At the mid-pulse instant t_1 of the first vector, the comparison between u_b and $u_{c2}/2$ yields C_{Aout} = L; at the mid-pulse instant t_2 of the second vector, the comparison between u_a and $u_{c2}/2$ yields C_{Bout} = H. At the end instant t_3 of the third vector, the measured current magnitudes are $|i_a|$ = 47.6 A and $|i_b|$ = 22.7 A.

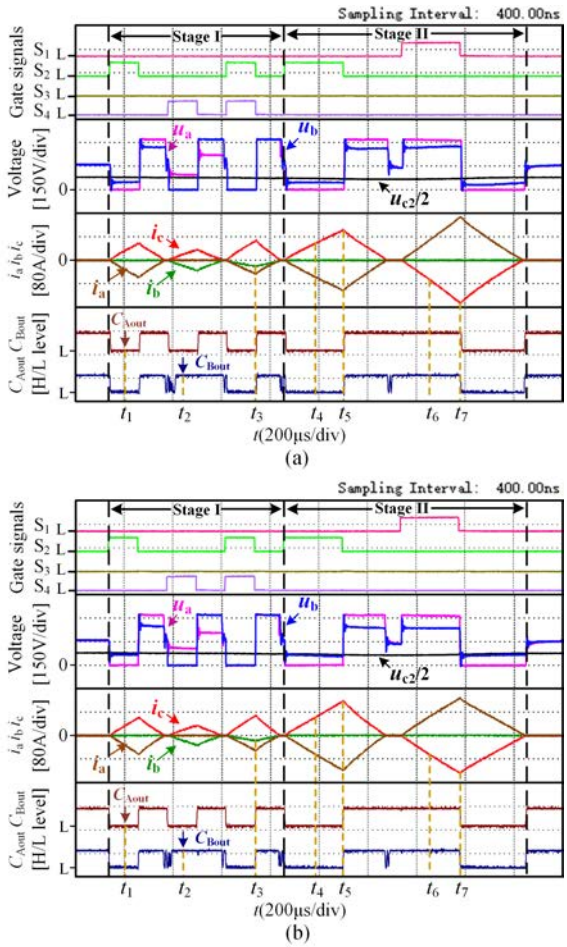

Fig. 14. Experimental waveforms of the proposed method at different initial rotor positions. (a) Located at 115° (2.01 rad). (b) Located at 295° (5.15 rad).

Based on the inductance-angle characteristics in Fig. 5, these results correspond to the ordering $L_b > L_c > L_a$, which localizes the rotor to either sector $90° < \theta < 120°$ or sector $270° < \theta < 300°$.

To determine the rotor polarity, two opposite vectors $\boldsymbol{V}(0100)$ and $\boldsymbol{V}(1000)$ are subsequently applied with a duration and interval of 240 μs. Based on the phase currents measured at the mid-pulse and end instants of the two pulses, the current slopes k_1, k_2, k_4, and k_5 (corresponding to t_4, t_5, t_6, and t_7, respectively) are calculated. The results indicate that $k_1 > k_2$ and $k_4 > k_5$. According to the decision rule, the rotor is finally identified as lying in the sector $90° < \theta < 120°$, i.e., Sector 4. The detailed initial position determination process is summarized in Table III.

TABLE III
THE INITIAL POSITION DETECTION PROCESS IN FIG. 14(A)

Initial position	115° (2.01 rad)				
Detection process	Stage I	$\boldsymbol{V}(0100)$	t_1	$u_b < u_{c2}/2$	C_{Aout} = L
		$\boldsymbol{V}(0001)$	t_2	$u_a > u_{c2}/2$	C_{Bout} = H
		$\boldsymbol{V}(0101)$	t_3	$\lvert i_a\rvert$ = 47.6 A $\lvert i_b\rvert$ = 22.4 A	$L_a > L_b$
	Stage II	$\boldsymbol{V}(0001)$	t_4	i_c = 58.2 A	$k_1 > k_2$
			t_5	i_c = 107.8 A	
		$\boldsymbol{V}(0010)$	t_6	i_c = −70.2 A	$k_4 > k_5$
			t_7	i_c = −147.3 A	
Result	Sector 4 ($90° < \theta < 120°$)				

Fig. 14(b) shows the experimental waveforms at the initial rotor position of 295° (5.15 rad). The detection process follows the same logic, and the waveform characteristics and calculated slopes are consistent with the expectations for the corresponding sector. The rotor is finally identified as lying in the sector $270° < \theta < 300°$, i.e., Sector 10. The detailed determination process is summarized in Table IV. In both cases of initial rotor positions at 115° (2.01 rad) and 295° (5.15 rad), the rotor remains stationary throughout the entire detection process, and no reverse motion is observed.

TABLE IV
THE INITIAL POSITION DETECTION PROCESS IN FIG. 14(B)

Initial position	295° (5.15 rad)				
Detection process	Stage I	$\boldsymbol{V}(0100)$	t_1	$u_b < u_{c2}/2$	C_{Aout} = L
		$\boldsymbol{V}(0001)$	t_2	$u_a > u_{c2}/2$	C_{Bout} = H
		$\boldsymbol{V}(0101)$	t_3	$\lvert i_a\rvert$ = 50.7 A $\lvert i_b\rvert$ = 20.1 A	$L_a > L_b$
	Stage II	$\boldsymbol{V}(0001)$	t_4	i_c = 56.7 A	$k_1 < k_2$
			t_5	i_c = 117.4 A	
		$\boldsymbol{V}(0010)$	t_6	i_c = −70.5 A	$k_4 < k_5$
			t_7	i_c = −131.4 A	
Result	Sector 10 ($270° < \theta < 300°$)				

To evaluate the proposed method over a full electrical revolution, detection experiments are carried out at 24 different initial rotor positions covering the range 0°–360°. Table V presents the correspondence between the detected sector index and the actual rotor position measured by the resolver, where the detected sector is consistent with the true rotor position. The proposed method provides an electrical

resolution of 30°, while in practical applications sensorless startup typically only requires the initial rotor position to be known within 60° electrical. Therefore, the detection performance of the proposed method is fully sufficient to meet the startup requirements of the FSTP BLDC drive.

TABLE V
THE DETECTION RESULT FOR DIFFERENT INITIAL ROTOR POSITIONS

Initial position	3.1° 26°	33.7° 55.8°	63.4° 85.2°	93.5° 115.4°
Detection result	Sector 1 ($0° < \theta < 30°$)	Sector 2 ($30° < \theta < 60°$)	Sector 3 ($60° < \theta < 90°$)	Sector 4 ($90° < \theta < 120°$)
Initial position	122.6° 145°	152.4° 174.7°	184° 204.6°	212.3° 235°
Detection result	Sector 5 ($120° < \theta < 150°$)	Sector 6 ($150° < \theta < 180°$)	Sector 7 ($180° < \theta < 210°$)	Sector 8 ($210° < \theta < 240°$)
Initial position	243.9° 265°	274° 295.1°	302.1° 324.8°	332.4° 354.1°
Detection result	Sector 9 ($240° < \theta < 270°$)	Sector 10 ($270° < \theta < 300°$)	Sector 11 ($300° < \theta < 330°$)	Sector 12 ($330° < \theta < 360°$)

D. *Motor Startup from Standstill*

To further verify the practical applicability of the proposed method in sensorless FSTP BLDC drives, a startup test from standstill is carried out at an initial rotor position within $60° < \theta < 90°$.

Fig. 15 shows the measured speed n, three-phase currents during the complete acceleration process. Based on the identified initial sector, the system applies the first optimal voltage vector and then transitions into the open-loop acceleration stage. When the rotor speed reaches 550 r/min and the back-EMF signal becomes clear, the control strategy switches to the sensorless closed-loop mode. Throughout the startup, the rotor accelerates in the correct direction without reverse rotation, and the speed response is smooth. These results demonstrate that the proposed initial rotor position detection method enables reliable sensorless startup for BLDC motors driven by an FSTP inverter.

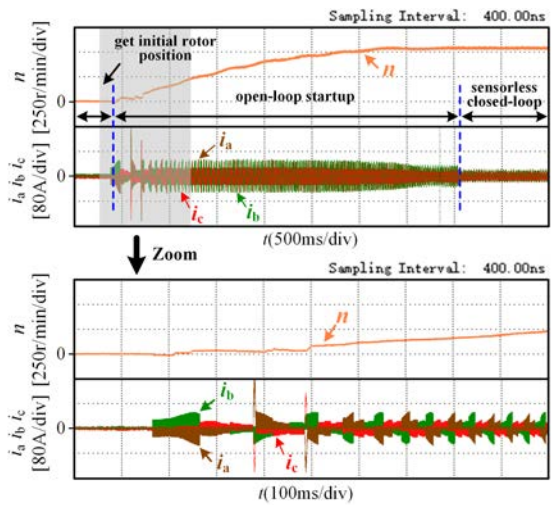

Fig. 15. The experimental waveforms of the motor start from a standstill when the actual rotor position is $60° < \theta < 90°$.

V. CONCLUSION

This paper has presented an initial rotor position detection method tailored to BLDC motors driven by an FSTP inverter, in which split DC-link capacitors and asymmetric voltage vectors render conventional SSTP strategies unreliable. By redesigning the detection pulse sequence specifically for the FSTP topology, the rotor position can be located within a 30° electrical sector without reverse rotation.

Compared with existing SSTP-oriented approaches, the distinctive value of this work lies in two aspects:

1) The impact of DC-link capacitor imbalance on FSTP voltage vectors is explicitly modeled, and only those vectors that remain robust under imbalance are used for detection.

2) The rotor sector and polarity are obtained through a combination of terminal-voltage comparison and intra-pulse current-slope evaluation, avoiding any reliance on ideal symmetric opposite vectors or DC-bus current comparison.

REFERENCES

[1] A. Khazaee, H. A. Zarchi, and G. A. Markadeh *et al.*, "MTPA Strategy for Direct Torque Control of Brushless DC Motor Drive," *IEEE Trans. on Ind. Electron.*, vol. 68, no. 8, pp. 6692–6700, Aug. 2021.

[2] P. Zheng, W. Liu, and Y. T. Gao *et al.*, "Review of Fault Diagnosis and Fault-tolerant Control Technologies for Permanent-magnet Synchronous Machine," *CES Trans. on Electr. Mach. and Syst.*, vol. 9, no. 3, pp. 320–339, Sept. 2025.

[3] P. Wang, Z. Q. Zhu, and N. M. A. Freire *et al.*, "Online Simultaneous Identification of Multi-parameters for Interior PMSMs Under Sensorless Control," *CES Trans. on Electr. Mach. and Syst.*, vol. 9, no. 4, pp. 422–433, Dec. 2025.

[4] G. Z. Zhang, M. H. Li, and X. Gu *et al.*, "Fault Diagnosis Method for Open-circuit Faults in NPC Three-level Inverter based on WKCNN," *CES Trans. on Electr. Mach. and Syst.*, vol. 9, no. 2, pp. 234–245, Jun. 2025.

[5] G. Burnand, A. Thabuis, and D. M. Araujo *et al.*, "Novel Optimized Shape and Topology for Slotless Windings in BLDC Machines," *IEEE Trans. on Ind. Appl.*, vol. 56, no. 2, pp. 1275–1283, Mar.-Apr. 2020.

[6] L. Yang, Z. Q. Zhu, and H. Bin *et al.*, "Virtual Third Harmonic Back EMF-based Sensorless Drive for High-speed BLDC Motors Considering Machine Parameter Asymmetries," *IEEE Trans. on Ind. Appl.*, vol. 57, no. 1, pp. 306–315, Jan.-Feb. 2021.

[7] X. D. Song, B. C. Han, and K. Wang, "Sensorless Drive of High-speed BLDC Motors based on Virtual Third-harmonic Back EMF and High-precision Compensation," *IEEE Trans. on Power Electron.*, vol. 34, no. 9, pp. 8787–8796, Sept. 2019.

[8] H. B. Wang, and H. P. Liu, "A Novel Sensorless Control Method for Brushless DC Motor," *IET Electric Power Appl.*, vol. 3, no. 3, pp. 240–246, May 2009.

[9] P. Champa, P. Somsiri, and P. Wipasuramonton *et al.*, "Initial Rotor Position Estimation for Sensorless Brushless DC Drives," *IEEE Trans. on Ind. Appl.*, vol. 45, no. 4, pp. 1318–1324, Jul.-Aug. 2009.

[10] Y. Liu, M. Wang, and L. Y. Xu, "Sensorless Control of BLDC Motor from Zero to Low Speed based on Rotor Saliency," in *Proc. of 2014 IEEE Conf. and Expo Transp. Electr. Asia-Pacific (ITEC Asia-Pacific)*, Beijing, China, Aug. 2014, pp. 1–7.

[11] H. B. Wang, G. R. Chen, and J. L. Shi *et al.*, "Initial Rotor Position Estimation of BLDC based on Inductance Method," in *Proc. of 2011 Int. Conf. on Busin. Manag. and Electron. Informat.*, Guangzhou, China, May 2011, pp. 656–659.

[12] G. Xie, K. Y. Lu, and S. K. Dwivedi *et al.*, "Minimum-voltage Vector Injection Method for Sensorless Control of PMSM for Low-speed Operations," *IEEE Trans. on Power Electron.*, vol. 31, no. 2, pp. 1785–1794, Feb. 2016.

[13] L. Zhou, X. M. Li, and W. Chen *et al.*, "A Modified Method for Initial Rotor Position Detection of Brushless DC Motor based on Voltage Vector Injection," in *Proc. of 2021 IEEE 4th Student Conf. on Electr. Mach. and Syst.*, Huzhou, China, Dec. 2021, pp. 1–6.

[14] D. H. Zhou, X. Q. Li, and Y. Tang, "Multiple-vector Model-predictive Power Control of Three-phase Four-switch Rectifiers with Capacitor Voltage Balancing," *IEEE Trans. on Power Electron*., vol. 33, no. 7, pp. 5824–5835, Jul. 2018.

[15] J. D. Lu, Y. H. Hu, and X. K. Zhang *et al*., "High-frequency Voltage Injection Sensorless Control Technique for IPMSMs Fed by a Three-phase Four-switch Inverter with a Single Current Sensor," *IEEE/ASME Trans. on Mechatronics*, vol. 23, no. 2, pp. 758–768, Apr. 2018.

[16] M. E. Zarei, D. Ramirez, and C. V. Nicolas *et al*., "Three-phase Four-switch Converter for SPMS Generators based on Model Predictive Current Control for Wave Energy Applications," *IEEE Trans. on Power Electron.*, vol. 35, no. 1, pp. 289–302, Jan. 2020.

[17] J. Hang, J. B. Zhang, and H. Qin *et al*., "A Simplified Model Predictive Voltage Control for Three-phase Four-switch Inverter-fed PMSM Drives with Capacitor Voltage Offset Suppression and Current Ripple Reduction," *IEEE Trans. on Power Electron.*, vol. 38, no. 4, pp. 5154–5166, Apr. 2023.

[18] C. Zhu, Z. Y. Zeng, and R. X. Zhao, "Adaptive Suppression Method for DC-link Voltage Offset in Three-phase Four-switch Inverter-fed PMSM Drives," *Electron. Lett*., vol. 52, no. 17, pp. 1442–1444, Aug. 2016.

[19] J. Qu, and K. Li, "Model Predictive Direct Torque Control of a Three-phase Four-switch Inverter Induction Motor Driving System," in *Proc. of 12th IET International Conference on Advances in Power System Control, Operation and Management (APSCOM 2022)*, Hybrid Conference, Hong Kong, China, Nov. 2022, pp. 77–82.

[20] P. S. Wang, F. Niu, and L. L. Guo *et al*., "An Improved Double-vector Model Predictive Control Strategy for Four-switch Three-phase Inverter-fed Permanent Magnet Synchronous Motor based on Visualisation Analysis Considering DC Voltage Pulsation," *IET Electr. Power Appl*., vol. 18, no. 11, pp. 1638–1650, Nov. 2024.

[21] W. Chen, L. X. Zhu, and S. Wang *et al*., "Rotating Restart Method for TPFS Inverter-fed Sensorless PMSM Drive System based on Dual Effective Voltage Vectors Injection," *IEEE Transactions on Power Electronics*, vol. 39, no. 9, pp. 11708–11722, Sept. 2024.

[22] W. Chen, S. Wang, and X. M. Li *et al*., "A Reference Voltage Self-correction Method for Capacitor Voltage Offset Suppression of Three-phase Four-switch Inverter-fed PMSM Drives," *World Electr. Vehicle Journal*, vol. 13, no. 2, pp. 24, Jan. 2022.

[23] D. Sun, J. P. Su, and C. Sun *et al*., "A Simplified MPFC with Capacitor Voltage Offset Suppression for the Four-switch Three-phase Inverter-fed PMSM Drive," *IEEE Trans. on Ind. Electron.*, vol. 66, no. 10, pp. 7633–7642, Oct. 2019.

[24] J. Hang, J. B. Zhang, and H. Wu *et al*., "Model Predictive Control with Fixed Weighting Factor for Three-phase Four-switch Inverter-fed PMSM Drives Considering Capacitor Voltage Offset Suppression," *IET Electr. Power Appl.*, vol. 14, no. 13, pp. 2697–2706, Dec. 2020.

[25] Y. F. Han, X. Q. Wu, and G. F. He *et al*., "Nonlinear Magnetic Field Vector Control with Dynamic-variant Parameters for High-power Electrically Excited Synchronous Motor," *IEEE Trans. on Power Electron.*, vol. 35, no. 10, pp. 11053–11063, Oct. 2020.

Xinmin Li (Member, IEEE) was born in Hunan, China, in 1989. He received the B.S. degree in automation from University of Science and Technology Beijing, Beijing, China, in 2011, and the Ph.D. degree in electrical engineering from Tianjin University, Tianjin, China, in 2017.

He is currently a professor with the Zhejiang University Advanced Electrical Equipment Innovation Center, and also with the School of Electrical Engineering, Tiangong University, Tianjin, China. His research interests include electrical machines and motor drives, electric drive systems of electric vehicles, power electronics, and wind power technology.

Kun Liu was born in Sichuan, China, in 2001. He received the B.S. degree in electrical engineering and automation from Tiangong University, Tianjin, China, in 2023.

He is currently working toward the M.S. degree in electrical engineering from Tiangong University, Tianjin, China. His research interests include electrical machines, motor drives, and power electronics.

Lu Zhou was born in Anhui, China, in 1992. He received the B.S. degree in electrical engineering and automation from Tongling University, Tongling, China, in 2015, and the M.S. degree in instrument science and technology from Taiyuan University of Technology, Taiyuan, China, in 2018, and the Ph.D. degree in electrical engineering from Tianjin University, Tianjin, China, in 2024.

He is currently an engineer working at No. 43 Research Institute of China Electronics Technology Group Corporation, Hefei, China. His research interests include motor drives and power electronics.

Tingna Shi (Senior Member, IEEE) was born in Yuyao, China, in 1969. She received the B.S. and M.S. degrees from Zhejiang University, Hangzhou, China, in 1991 and 1996, respectively, and the Ph.D. degree from Tianjin University, Tianjin, China, in 2009, all in electrical engineering.

She is currently a professor with the College of Electrical Engineering, Zhejiang University. Her current research interests include electrical machines and their control systems, power electronics, and electric drives.

Wei Chen (Member, IEEE) was born in Shanxi, China, in 1977. He received the B.S., M.S., and Ph.D. degrees in electrical engineering from Tianjin University, Tianjin, China, in 2000, 2003, and 2006, respectively.

He is currently a professor with the School of Electrical Engineering, Tiangong University, Tianjin, China, and the Vice President with the National Local Joint Engineering Research Center of Electric Machine System Design and Manufacturing, Tianjin, China. His research interests include electrical machines and drivers, and power electronics.